

Soft Matter

Accepted Manuscript



This is an *Accepted Manuscript*, which has been through the Royal Society of Chemistry peer review process and has been accepted for publication.

Accepted Manuscripts are published online shortly after acceptance, before technical editing, formatting and proof reading. Using this free service, authors can make their results available to the community, in citable form, before we publish the edited article. We will replace this *Accepted Manuscript* with the edited and formatted *Advance Article* as soon as it is available.

You can find more information about *Accepted Manuscripts* in the [Information for Authors](#).

Please note that technical editing may introduce minor changes to the text and/or graphics, which may alter content. The journal's standard [Terms & Conditions](#) and the [Ethical guidelines](#) still apply. In no event shall the Royal Society of Chemistry be held responsible for any errors or omissions in this *Accepted Manuscript* or any consequences arising from the use of any information it contains.

Concentration-induced planar-to-homeotropic anchoring transition of stiff ring polymers on hard walls

Peter Poier,^a Sergei A. Egorov,^{b,c} Christos N. Likos^{a,c} and Ronald Blaak^{*a}

Received Xth XXXXXXXXXXXX 20XX, Accepted Xth XXXXXXXXXXXX 20XX

First published on the web Xth XXXXXXXXXXXX 200X

DOI: 10.1039/b000000x

We study the structure and interfacial ordering of stiff rings polymers close to repulsive walls. For this purpose, we employ an anisotropic effective model in which the rings are pictured as soft, penetrable discs [P. Poier, C. N. Likos, A. J. Moreno and R. Blaak, *Macromolecules* **48**, 4983 (2015)]. We have studied this model in the bulk and in the presence of a wall, employing Density Functional Theory and computer simulations. While the Ornstein Zernike Equation in combination with the Hypernetted Chain Approximation gives results that are in quantitative agreement with computer simulations, a simple Mean Field approximation strongly overestimates the interaction between the effective particles in the bulk. We discover that by increasing density one can induce a reorientation of the effective rings in the vicinity of a wall, which prefer to orient themselves parallel to the surface (face-on or *planar*) for low densities ρ and reorient orthogonal to the wall (edge-on or *homeotropic*) for higher values of ρ . This transition in the surface-structure can be observed in both computer simulations, as well as in an appropriate Density Functional Theory. We trace its physical origin in the penetrable character of the rings, which allow for a reduction of the surface tension contribution due to ring-ring interactions upon the emergence of homeotropic ordering on the wall upon increasing the density of the system.

1 Introduction

A detailed microscopic understanding of the structural, thermodynamic, and dynamic behavior of soft matter systems confined in nanopores and slits of various geometry is of both fundamental and practical importance^{1,2}. One particular example of such confined soft matter systems involves disc-shaped particles in various pores³, which are essential for understanding confined discotic liquid crystals⁴ and, as such, have been extensively studied via experiments² computer simulations^{5–8}, and theory^{3,8–10}.

The primary focus of the above studies has been on the ordering and surface tension of the disc-shaped particles at the confining surface and the concomitant effect of the geometrical confinement on the isotropic-nematic-columnar phase behavior of the corresponding liquid crystal. In particular, it has been shown that both the shape of the particles⁵ and the wall-particle interaction potential^{6,7} strongly affect the observed surface ordering. More specifically, for disc-shaped particles confined in a planar slit, two types of wall ordering are typically distinguished¹¹: planar anchoring (or “edge-on”, with the director parallel to the wall) and homeotropic anchoring

(or “face-on”, with the director normal to the wall). Clearly, the ability to control and switch the type of anchoring is crucial for developing practical applications of confined discotic liquid crystals, such as optical compensation films⁴. From the experimental point of view² the two most common control parameters that can be used to control the anchoring type are temperature and density. The former parameter can be used to tune the strength of the wall-particle interaction. Along these lines, it has been shown⁷ that switching from a hard wall (which excludes the particles completely) to an “adsorbent” wall (which excludes only the centers of mass of the particles) promotes switching of surface ordering of disc-shaped particles from homeotropic to planar. Concomitantly, the hard walls facilitate isotropic-nematic transition relative to the bulk (capillary nematization), while adsorbent walls delay this transition (capillary isotropization). By contrast, using the density as the control parameter was shown to have little to no effect on the surface ordering⁵. In this connection, it is important to emphasize that all the aforementioned studies have modeled the disc-shaped particles either as strictly hard (completely impenetrable) objects^{5,7,8} or as (only slightly) softer repulsive entities⁶ of the type corresponding to Gay-Berne¹² oblate ellipsoids. In the case of ultrasoft interaction-potentials employed in modeling macroparticles one would expect a much stronger effect of density on surface-ordering. The purpose of the present work is to study precisely such a system.

Our microscopic model is based on recently obtained

^a Faculty of Physics, University of Vienna, Boltzmanngasse 5, A-1090, Vienna, Austria, E-mail: ronald.blaak@univie.ac.at

^b Department of Chemistry, University of Virginia, McCormick Road, P.O. Box 400319, Charlottesville, VA, United States

^c Erwin Schrödinger International Institute for Mathematics and Physics, University of Vienna, Boltzmanngasse 9, A-1090 Vienna, Austria

anisotropic effective pair potentials, which were introduced in order to coarse-grain semiflexible ring polymers of various chain lengths¹³, whereby each ring was represented by a soft penetrable disc. The model has been validated by comparing its structural predictions in the bulk with the corresponding results of full monomer-resolved computer simulations. It was shown that for the short- and intermediate-length ring polymers, with a contour- to persistence-length ratio of $l/l_p \cong 6.7$, the model is capable of reproducing the essential structural properties of a bulk system nearly quantitatively, while the longer rings (at high concentrations) were shown to undergo conformational changes which cannot be reproduced by an effective anisotropic soft-disc model. Accordingly, in the present study we consider precisely those soft discs which mimic intermediate-length ring polymers with $l/l_p \cong 6.7$ and focus on their structural properties and self-organization under confinement between planar walls.

Clearly, any systematic study of a confined system requires the knowledge of its corresponding behavior in the bulk as a reference. In this connection, it is important to note that the aforementioned simulation study¹³ of the bulk system has shown no indication of neither an isotropic-nematic nor an isotropic-columnar ordering phase transition, at least in the density range that was considered. This is in contrast to another anisotropic effective potential between soft disclike particles which has been proposed to model interactions between core-corona disc-shaped micelles¹⁴. The bulk phase behavior of this system was studied via dissipative particle dynamics simulations, and a transition from the isotropic to the hexagonal columnar phase was found at sufficiently high densities¹⁴. This difference in the phase behavior is likely due to the fact that the model pair potential used in Ref.¹⁴ is significantly different from the one employed here, in that its form was not derived based on the atomistic simulations of the corresponding monomer-resolved system, but rather simply postulated. As a result, this model potential does not distinguish between the two soft discs approaching each other “edge-to-edge” and “edge-to-face” while in the present model the corresponding effective interactions are very different.

Given the absence of the ordering phase transitions in the bulk for our model, we instead focus on the anchoring type and surface tension of the disc-shaped particles at the confining wall. We address these two problems by employing a combination of computer simulations and density functional theory (DFT). Both methods have their advantages and disadvantages and therefore can be used in a complementary fashion. Thus, simulations, at least in principle, produce exact results for a given microscopic model, except for the inevitable statistical noise. However, this advantage comes at a high computational cost, because very long runs are required in order to reduce the noise level. By contrast, DFT calculations are relatively cheap, but involve unavoidable approximations. Hence, the

accuracy of the DFT predictions must be tested and validated by comparison with computer simulations. Another significant advantage of the DFT approach comes from the fact that this method is based on minimizing the free energy, and, as such, allows a straightforward determination of various thermodynamic observables, which are notoriously difficult to obtain from computer simulations. For example, it is very computationally demanding to obtain surface tension of semiflexible polymers at a hard wall from simulations, while in DFT this quantity can be calculated relatively easily¹⁵. In view of the above, in the present work we employ a judicious combination of these two methods. Specifically, given the availability of extensive simulation results for the bulk coarse-grained system¹³, we begin by developing and testing the DFT approach in the bulk. The anisotropic total and direct pair correlation functions in the bulk are obtained by combining the hypernetted chain (HNC) closure with the Percus method of treating one given disc as a “test particle” exerting the external potential (simply the effective coarse-grained pair potential in this case) on all the other discs¹⁶. Once the simulation and DFT predictions for the pair distribution functions are compared and the accuracy of the DFT in the bulk is confirmed, we proceed to study the structural properties of the confined system.

In order to carry out the DFT calculations in confinement, we use the bulk direct pair correlation functions as input, treat the hard planar confining wall(s) as the source of the external potential, and compute the wall-induced one-particle density of rings. For spherical particles such an approach has been previously successfully used to study the distribution of spherical solvents around two colloids^{17,18}. Once again, the accuracy of the DFT method is confirmed by direct comparison with the simulation results. Our key finding for the confined system is that the surface ordering of the soft discs at a hard planar wall switches from homeotropic to planar with increasing density. This interesting and important effect was observed both in computer simulations and in DFT and is in stark contrast to confined hard discs, where, as mentioned earlier, density has little effect on the type of surface anchoring, and the latter is largely controlled by the wall-disc interaction potential (in the present case, only hard walls are considered).

The remainder of the paper is organized as follows. In Section 2 we briefly review our coarse-grained model of effective potentials between soft discs originally devised to mimic the interactions between semiflexible ring polymers as well as the effective interactions of the rings with the planar walls. In Section 3 we provide technical details on the computer simulations and describe the DFT approach employed in the present work. Section 4 deals with simulation and DFT results for the bulk system of soft discs, while in Section 5 the confining effect of planar hard walls is studied. Finally, our conclusions are summarized in Section 6, whereas a brief discussion of

the underlying monomer-resolved simulation model and some technical details on the DFT implementation are relegated to the Appendices.

2 Coarse-Grained Ring Polymer Model

In ref.¹³ we have developed an effective model for the simulation of semiflexible ring-polymers, where these macroparticles are described as penetrable disc-like objects given by their position \mathbf{r} and director \mathbf{d} pointing into the direction orthogonal to the conceived disc; the latter is by construction a unit vector, $|\mathbf{d}| = 1$, and it corresponds to the direction of the eigenvector corresponding to the smallest eigenvalue of the gyration tensor¹³. The interaction potential in this coarse grained description was derived from the anisotropic pair-correlation function $g(r, \cos \theta_1, \cos \theta_2, \varphi)$ between two monomer-resolved ring polymers at infinite dilution via the equation

$$\beta V_{\text{eff}}(r, \cos \theta_1, \cos \theta_2, \varphi) = -\ln[g(r, \cos \theta_1, \cos \theta_2, \varphi)], \quad (1)$$

where r describes the distance between the centers of mass of the ring polymers and the angles $\cos \theta_1, \cos \theta_2, \varphi$ their relative orientation:

$$\begin{aligned} \cos \theta_1 &\equiv \mathbf{d}^{(1)} \cdot \hat{\mathbf{r}}; \\ \cos \theta_2 &\equiv \mathbf{d}^{(2)} \cdot \hat{\mathbf{r}}; \\ \varphi &\equiv \arccos \left(\frac{\mathbf{d}_{\perp}^{(1)} \cdot \mathbf{d}_{\perp}^{(2)}}{|\mathbf{d}_{\perp}^{(1)}| |\mathbf{d}_{\perp}^{(2)}|} \right). \end{aligned} \quad (2)$$

In Eq. (2) above, $\hat{\mathbf{r}} \equiv \mathbf{r}/r$ is the unit vector along the line connecting the centers of mass of the two rings, $\mathbf{d}^{(i)}$, $i = 1, 2$ is the director of the i -th ring and

$$\mathbf{d}_{\perp}^{(i)} = \mathbf{d}^{(i)} - (\mathbf{d}^{(i)} \cdot \hat{\mathbf{r}}) \hat{\mathbf{r}} \quad (3)$$

is the component of $\mathbf{d}^{(i)}$ perpendicular to the vector \mathbf{r} connecting the two centers.

Details concerning the underlying monomer resolved model lying monomer resolved model and the numerical computation of the anisotropic pair-correlation function are briefly recapped in Appendix A and for the numerical computation of the anisotropic pair-correlation function we refer the reader to ref.¹³. While it is impossible to visualize the entire four-dimensional effective interaction potential one can obtain an intuitive understanding of the interaction by concentrating on particular fixed orientations between the rings. In Fig. 1 we show three characteristic orientations of two interacting rings and we introduce the notation for the same. In Fig. 2 we plot the effective interaction for these main fixed orientations, together with the rotationally averaged, isotropic effective potential. In the abscissa of the plot, distances between the particles are denoted in multiples of the rings' diameter of gyra-

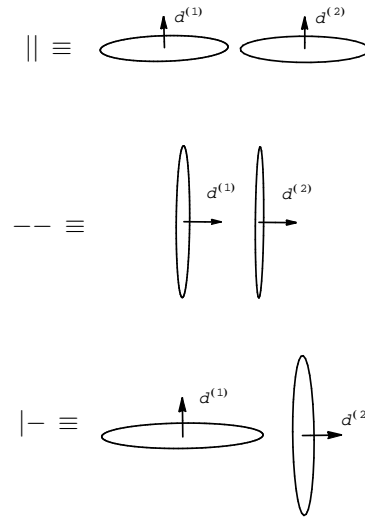


Fig. 1 The three distinct orientations of effective rings, along with the corresponding notation. At the top, the symbol $||$ denotes an orientation in which the directors of the two rings are parallel to each other and perpendicular to the vector connecting the ring centers. In the middle panel, the notation $--$ denotes rings with directors parallel to each other and to the connecting vector. Finally, the notation $|-$ at the bottom panel denotes rings with mutually perpendicular directors, one of which is parallel to the connecting vector and other parallel to it. The accompanying sketches visualize the corresponding arrangements.

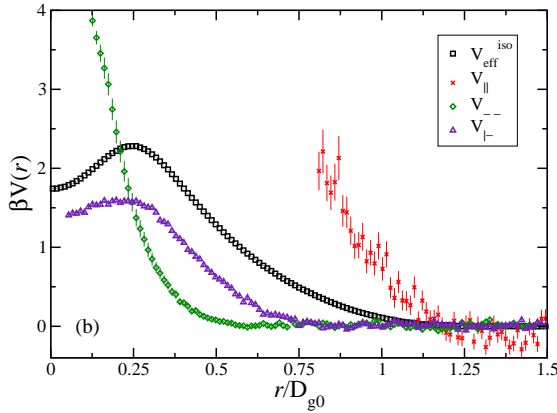


Fig. 2 The effective potential for three different, fixed configurations of the directors and the connecting vector. As a comparison we also plot the pair potential in the isotropic effective potential $\beta V_{\text{eff}}^{\text{iso}}(r) = -\ln g(r)$, where $g(r)$ is the orientation-averaged radial distribution function of the system. The effective potentials are shown only for r values for which we have relatively good statistics.

tion at infinite dilution, $D_{g0} \approx 13.3\sigma$ for the rings of $N = 50$ monomers¹³ of monomer size σ .

When r approaches D_{g0} from above, the potential $V_{||}(r)$ increases significantly, while $V_{--}(r)$ stays close to 0. Imagining the rings as discs with diameter D_{g0} this result is quite intuitive. In the $||$ configuration, the rings lie in the same plane and will therefore start to overlap as soon as $r \leq D_{g0}$. As the rings are not perfect circles and their shape fluctuates, they can feel each other also for distances r which are slightly larger than D_{g0} . In the $--$ configuration two discs overlap only if the distance between their centers of mass is smaller than their thickness. However, as soon as the rings can overlap in $--$ type configurations the effective potential increases very fast for smaller r . This is the regime where the $|-$ orientation is more favorable since the corresponding microscopic configurations are interpenetrating rings which are only suppressed by a relatively small bending energy term.

We have carried out Molecular Dynamics simulation of a monomer-resolved ring in the presence of a wall to determine the effective ring-wall potential. To this end, we have employed the same methods and the same underlying model for the monomer resolved rings as in ref.¹³. For the monomer-wall interaction potential we have used

$$V_{\text{wall}}(z) = \begin{cases} \varepsilon \left[\frac{2}{15} \left(\frac{\sigma}{z}\right)^9 - \left(\frac{\sigma}{z}\right)^3 + \frac{\sqrt{10}}{3} \right] & \text{if } z < \left(\frac{2}{5}\right)^{1/6} \sigma; \\ 0 & \text{if } z \geq \left(\frac{2}{5}\right)^{1/6} \sigma, \end{cases} \quad (4)$$

where z denotes the distance of the monomer to the wall. The energy scale ε and the length σ also appear in the Lennard-Jones interaction between monomers in the monomer-resolved ring-polymer model. If the space for $z < 0$ was filled with a homogeneous distribution of Lennard Jones interaction sites with density $\pi\rho\sigma^3/6 = 1$, $V_{\text{wall}}(z)$ without the cutoff would describe the force that a particle feels for $z > 0$. We have introduced the cutoff such that the wall potential is purely repulsive.

For a system containing only one wall and a single ring polymer we have obtained a distribution function $P_{\text{wall}}(z, \mathbf{d} \cdot \hat{\mathbf{z}})$ that is proportional to the probability that the center of mass of the ring is found a distance z away from the wall, and that the scalar product of its director \mathbf{d} with the vector normal to the wall is $\mathbf{d} \cdot \hat{\mathbf{z}}$. The normalization is given by $P_{\text{wall}} = 1$ for $z \rightarrow \infty$; in particular, calling $p(z, \mathbf{d} \cdot \hat{\mathbf{z}})$ and $p_{\text{id}}(z, \mathbf{d} \cdot \hat{\mathbf{z}})$ the probability densities of finding a ring at $(z, \mathbf{d} \cdot \hat{\mathbf{z}})$ in the presence and absence of the wall, respectively, $P_{\text{wall}}(z, \mathbf{d} \cdot \hat{\mathbf{z}})$ is defined as the ratio:

$$P_{\text{wall}}(z, \mathbf{d} \cdot \hat{\mathbf{z}}) = \frac{p(z, \mathbf{d} \cdot \hat{\mathbf{z}})}{p_{\text{id}}(z, \mathbf{d} \cdot \hat{\mathbf{z}})}. \quad (5)$$

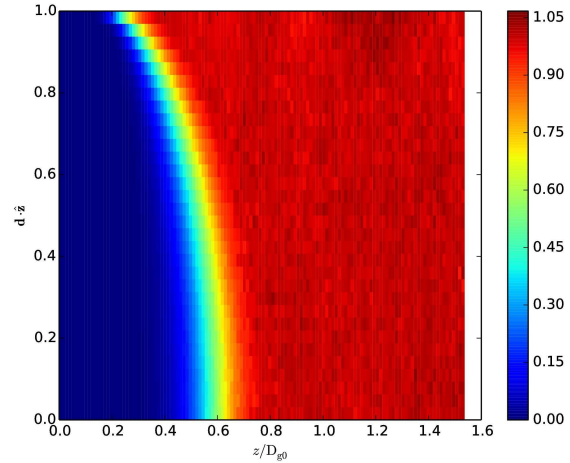


Fig. 3 Visualization of the function $P_{\text{wall}}(z, \mathbf{d} \cdot \hat{\mathbf{z}})$, which is proportional to the probability that a single ring polymer is located a distance z away from the wall and that the scalar product of its director \mathbf{d} with the vector normal to the wall is $\mathbf{d} \cdot \hat{\mathbf{z}}$.

The distribution is visualized in Fig. 3 and its behavior of P_{wall} is quite intuitive: The center of mass of rings with a director orthogonal to the wall (“face-on”) can come closer to the wall than rings with a director parallel to the wall (“edge-on”). For rings with a director parallel to the wall, the range where P_{wall} is between 0 and 1 is larger than for rings with an orthogonal director. The reason for this is that rings with their director standing parallel to the wall can be squeezed which

makes it possible for their center of mass to come closer to the wall. However the squeezing also costs energy and thus the probability for these squeezed states is suppressed. Therefore, there is a range of wall-distances, corresponding to squeezed states of the rings, for which P_{wall} is between 0 and 1. While individual monomers can approach the wall up to the distance $(\frac{2}{5})^{1/6} \sigma \approx 0.066D_{g0}$ without feeling any energy penalty from the wall, even rings with their director standing orthogonal to the wall have a very small probability to approach the wall closer than $0.2D_{g0}$, because the entropy of the allowed configurations of the monomers of a ring is significantly affected if its center of mass is held very close to the wall. The wall is purely repulsive, and thus values of the function $P_{\text{wall}}(z, \mathbf{d} \cdot \hat{\mathbf{z}})$ are, within numerical accuracy, lower or equal to unity. In the anisotropic effective model we then employ the effective potential

$$\beta\Phi_{\text{wall}}(z, \mathbf{d} \cdot \hat{\mathbf{z}}) = -\ln P_{\text{wall}}(z, \mathbf{d} \cdot \hat{\mathbf{z}}) \quad (6)$$

to describe the interaction between a ring polymer and the wall. In Fig. 4 this potential is visualized for a homeotropic and a planar orientation of the effective disc-like particle with respect to the wall.

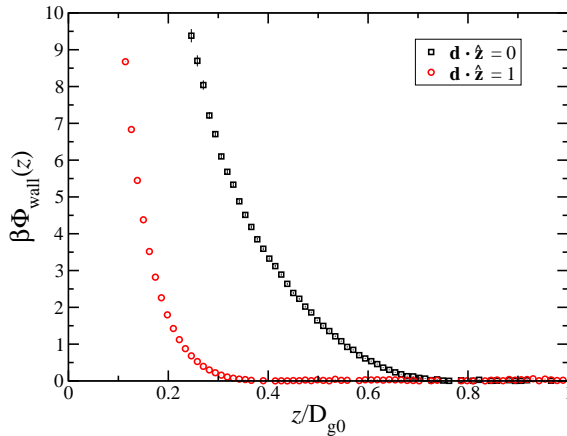


Fig. 4 The ring-wall interaction potential in the effective model Φ_{wall} for a homeotropic ($\mathbf{d} \cdot \hat{\mathbf{z}} = 0$) and a planar ($\mathbf{d} \cdot \hat{\mathbf{z}} = 1$) orientation of the ring with respect to the wall.

3 Details on Density Functional Theory and Monte Carlo simulations

A system of disc like particles, described by their position \mathbf{r} and their director \mathbf{d} , can be interpreted as a special case of a

system of point-like particles with one particle type for each director orientation \mathbf{d} . To investigate the structure of the fluid, both in the bulk and under confinement, we employ both Density Functional Theory (DFT) and Monte Carlo computer simulations. In what follows, we present the main ingredients of these approaches and their implementation, leaving some technical details for Appendix B.

Integral equation theories are usually employed to investigate the (pair) structure of uniform, classical fluids^{16,19}. We have applied the Ornstein-Zernike equation (OZE) together with the Hypernetted Chain (HNC) approximation closure for anisotropic, effective interactions to obtain two coupled integral equations, the OZE

$$h(\mathbf{r}, \mathbf{d}^{(1)}, \mathbf{d}^{(2)}) - c(\mathbf{r}, \mathbf{d}^{(1)}, \mathbf{d}^{(2)}) = \frac{\rho}{4\pi} \int d\Omega \int dx c(\mathbf{x}, \mathbf{d}^{(1)}, \mathbf{d}) h(\mathbf{r} - \mathbf{x}, \mathbf{d}, \mathbf{d}^{(2)}), \quad (7)$$

and the HNC closure,

$$h(\mathbf{r}, \mathbf{d}^{(1)}, \mathbf{d}^{(2)}) + 1 = \exp \left[-\beta V_{\text{eff}}(\mathbf{r}, \mathbf{d}^{(1)}, \mathbf{d}^{(2)}) \right] \times \exp \left[h(\mathbf{r}, \mathbf{d}^{(1)}, \mathbf{d}^{(2)}) - c(\mathbf{r}, \mathbf{d}^{(1)}, \mathbf{d}^{(2)}) \right], \quad (8)$$

which must be solved self-consistently to obtain the total and direct correlation functions $h(\mathbf{r}, \mathbf{d}^{(1)}, \mathbf{d}^{(2)})$ and $c(\mathbf{r}, \mathbf{d}^{(1)}, \mathbf{d}^{(2)})$ respectively. In Eq. (7) above, the integral $\int d\Omega$ is carried over the polar and azimuthal angles of the director \mathbf{d} .

The HNC can be formally derived from a more general scheme, namely from DFT of inhomogeneous fluids²⁰. The key ingredient is to consider a particle of the fluid clamped at the origin and acting to the bulk of the fluid as an external field, giving rise to an inhomogeneous density. As shown by Percus²¹, this density profile is just the product between the bulk density and the radial distribution function $g(\mathbf{r}, \mathbf{d}^{(1)}, \mathbf{d}^{(2)}) \equiv h(\mathbf{r}, \mathbf{d}^{(1)}, \mathbf{d}^{(2)}) + 1$. Accordingly, each different choice of the functional for the excess free energy determines a different closure. In particular, an excess free energy functional quadratic to the deviation of the inhomogeneous density from its bulk value gives rise to the HNC approximation²².

Since the anisotropic effective interaction $V_{\text{eff}}(\mathbf{r}, \mathbf{d}^{(1)}, \mathbf{d}^{(2)})$ is soft and penetrable, we also apply here a related closure, put forward for ultrasoft isotropic interactions, the Mean Field Theory (MFT), which is also based on a quadratic form of the excess functional²³ but with the additional approximation of relating the direct correlation function to the interaction potential via:

$$c(\mathbf{r}, \mathbf{d}^{(1)}, \mathbf{d}^{(2)}) = -\beta V_{\text{eff}}(\mathbf{r}, \mathbf{d}^{(1)}, \mathbf{d}^{(2)}). \quad (9)$$

Combining this expression with the Percus test-particle approach, we obtain the MFT-closure for the pair correlation

function:

$$h(\mathbf{r}, \mathbf{d}^{(1)}, \mathbf{d}^{(2)}) + 1 = \exp \left[-\beta V_{\text{eff}}(\mathbf{r}, \mathbf{d}^{(1)}, \mathbf{d}^{(2)}) \right] \times \exp \left[-\frac{\beta \rho}{4\pi} \int d\Omega \int d\mathbf{r}' V_{\text{eff}}(\mathbf{x}, \mathbf{d}^{(1)}, \mathbf{d}) h(\mathbf{r} - \mathbf{x}, \mathbf{d}, \mathbf{d}^{(2)}) \right]. \quad (10)$$

We have solved Eqs. (7)-(8) and (10) numerically by the iterative procedure explained in Appendix B. In the bulk, we obtain the distribution function $g(\mathbf{r}, \mathbf{d}^{(1)}, \mathbf{d}^{(2)}) \equiv h(\mathbf{r}, \mathbf{d}^{(1)}, \mathbf{d}^{(2)}) + 1$; in what follows, we will be showing results for a reduced quantity, the radial distribution function $g(r)$, which arises from the former by averaging over the orientations of both directors $\mathbf{d}^{(1)}$ and $\mathbf{d}^{(2)}$, namely:

$$g(r) = \frac{1}{(4\pi)^2} \int \int d\Omega_1 d\Omega_2 g(\mathbf{r}, \mathbf{d}^{(1)}, \mathbf{d}^{(2)}). \quad (11)$$

In the presence of a wall we have used DFT and Monte Carlo simulations to predict the one-particle density of the soft discs, $\rho^{(1)}(z, \cos \theta)$, as a function of the distance z from the wall and the angle $\theta = \cos^{-1}(\mathbf{d} \cdot \hat{\mathbf{z}})$ between the unit vector $\hat{\mathbf{z}}$ and the disc director \mathbf{d} . For the DFT calculation of the density profile of the fluid, we have employed the same quadratic excess free energy functional that leads to the HNC in the bulk; this time the full free energy functional includes the contribution from the interaction with the wall potential $\Phi_{\text{wall}}(z, \cos \theta)$. It follows that the inhomogeneous density $\rho^{(1)}(z, \cos \theta)$ is determined from the following self-consistent equation:

$$\rho^{(1)}(z, \cos \theta) = \frac{\rho}{4\pi} \exp[-\beta \Phi_{\text{wall}}(z, \cos \theta)] \times \exp \left[\int d \cos \theta' dz' \Delta \rho^{(1)}(z', \cos \theta') \bar{c}(z - z', \cos \theta, \cos \theta') \right], \quad (12)$$

where ρ is the bulk density, far away from the wall, and we also define the deviation of the density profile from the bulk value:

$$\Delta \rho^{(1)}(z', \cos \theta') = \rho^{(1)}(z', \cos \theta') - \rho, \quad (13)$$

and the laterally-averaged direct correlation function:

$$\bar{c}(z, \cos \theta, \cos \theta') = \int dx' dy' d\phi' c(x', y', z, \mathbf{d}, \mathbf{d}'), \quad (14)$$

with (θ', ϕ') being the polar and azimuthal angles of the director \mathbf{d}' . In order to use Eq. (12) we need to know the direct correlation function $c(\mathbf{r}, \mathbf{d}, \mathbf{d}')$ at the bulk density ρ , which we consistently obtain from the numerical solution of the HNC-closure in the bulk, Eqs. (7) and (8). To solve the self-consistent equation (12), we have again used the iterative procedure described in Appendix B, where we have set

$\rho^{(1)}(z, \cos \theta)$ equal to the bulk density ρ for $z > 4D_{g0}$. Finally, we note that, in full analogy with the bulk case, the formal substitution of Eq. (9) into Eq. (12) gives rise to the MFT for confined systems.

In our Monte Carlo simulations, we have simulated a total of 3200 coarse-grained ring-polymers between two walls. To perform a comparison to the DFT results obtained for a single wall, we set the two walls apart by a distance of $L_z = 7.7D_{g0}$, which is sufficiently large to obtain bulk behavior in the middle of the simulation box. We have then superimposed the density distributions measured for $z \in [0, L_z/2]$ and $z \in [L_z/2, L_z]$ to obtain the simulation result for $\rho^{(1)}(z, \cos \theta)$ for $z \in [0, L_z/2]$ in the presence of one wall. We have always started the simulations with initial configurations where the positions and the directors of the particles were generated randomly and we have employed a total of 2×10^9 MC moves to equilibrate the system. We have employed single particle MC moves, which randomly displaced and rotated individual effective particles.

4 Bulk structure: Theory vs. simulation

It has been previously demonstrated¹³ that the coarse-grained model faithfully reproduces the pair correlation structure of the system in comparison with monomer-resolved simulations for densities as high as $\rho^* \cong 10$. Accordingly, we focus in what follows exclusively on the question of the validity of certain theoretical approximations to the determination of the pair correlations of the coarse-grained model. To put these theoretical approximations to the test, we have performed extensive measurements of various structural quantities and set them against the results obtained for the same in the MC simulations carried out in ref.¹³. We have restricted ourselves to densities $\rho^* \leq 7$, where we introduce the quantity $\rho^* \equiv \rho D_{g0}^3$ as a dimensionless measure of the density ρ .

We first present, in Fig. 5, results for the angular-averaged pair distribution function $g(r)$ for $\rho^* = 1$ and $\rho^* = 3$. The HNC is in full agreement with simulation, whereas the results from MFT are clearly inferior. One reason why the MFT is unsuccessful in making accurate predictions is that the anisotropic interaction potential is in fact not soft everywhere, but can become very high and steep for certain relative orientations of the rings, as we have seen in Fig. 2. This renders the MFT less accurate, because it assumes that for every configuration the distribution of other particles around a selected one is given by the anisotropic pair correlation function $g(\mathbf{r}, \mathbf{d}^{(1)}, \mathbf{d}^{(2)})$. This, however, leads to big interaction energies between particles in the vicinity of the selected one, since according to the MFT approximation they can assume orientations with respect to each other that involve very high energies. For this reason, we should expect MFT to overestimate the strength of the interaction between the particles, and we

can indeed see from our results that at a given density ρ^* MFT predicts a $g(r)$ that looks similar to the result which the MC simulation obtains at a higher density. Another reason why MFT might be in general worse for systems where the particles can orient in different directions is that we now not only assume that the overall number of particles in a thin spherical shell around a reference particle is always identical but that this is true for the number of each possible particle orientation individually. This is of course an even stronger statement than the assumption of MFT in the isotropic system, where there is only one particle type. The results of HNC on the other hand are in very good agreement with simulations; this agreement persists also at much higher densities, as can be seen in particular in the two top sets of curves in Fig. 5 for the densities $\rho^* = 5$ and $\rho^* = 7$. Here, no MFT-results are shown because this approximation does not converge at such densities.

From the full, anisotropic pair correlation function $g(\mathbf{r}, \mathbf{d}^{(1)}, \mathbf{d}^{(2)})$, we can also extract useful information about the orientational correlations of the particles in the system. In particular, we are interested in the probability distribution for the scalar products between the directors $\mathbf{d}^{(1)}$ and $\mathbf{d}^{(2)}$ of two effective particles which are a distance $r < 0.6D_{g0}$ away from each other, to which we will refer to as $P(\mathbf{d}^{(1)} \cdot \mathbf{d}^{(2)})$ in the following. Results for $P(\mathbf{d}^{(1)} \cdot \mathbf{d}^{(2)})$ from theory and MC simulations of the effective system with anisotropic interaction are shown in Fig. 6 for $\rho^* = 1$ and $\rho^* = 3$. As for the angular-averaged pair correlation function $g(r)$, the HNC approximation is in excellent agreement with the results from MC simulations and correctly predicts the small change of $P(\mathbf{d}^{(1)} \cdot \mathbf{d}^{(2)})$ from density $\rho^* = 1$ to $\rho^* = 3$, while there are significant deviations for the MFT prediction. The two sets of top curves in Fig. 6 show the results for $P(\mathbf{d}^{(1)} \cdot \mathbf{d}^{(2)})$ at the higher densities $\rho^* = 5$ and $\rho^* = 7$. Once more, the HNC results are in excellent agreement with MC simulations and they show the propensity of the soft discs around an arbitrary disc to orient themselves parallel to the former. The fluid displays short-range orientational correlations, expressed by the propensity of the rings to organize into one-dimensional stacks^{13,24,25}. We emphasize, however, that overall the fluid of the stiff rings is, at these densities, isotropic. No sign of a nematic or columnar order has been found in the simulations or in theory, although the failure of the MFT to converge might point to an instability of the isotropic phase at higher densities.

We have thus seen that the HNC approximation is able to accurately predict the two observables $g(r)$ and $P(\mathbf{d}^{(1)} \cdot \mathbf{d}^{(2)})$ for the system with anisotropic effective interactions. On the basis of the excellent performance of the HNC in the bulk, we follow up in the next section on these promising results, to make DFT-predictions for the distribution of discs in the presence of a wall and test them against MC simulations.

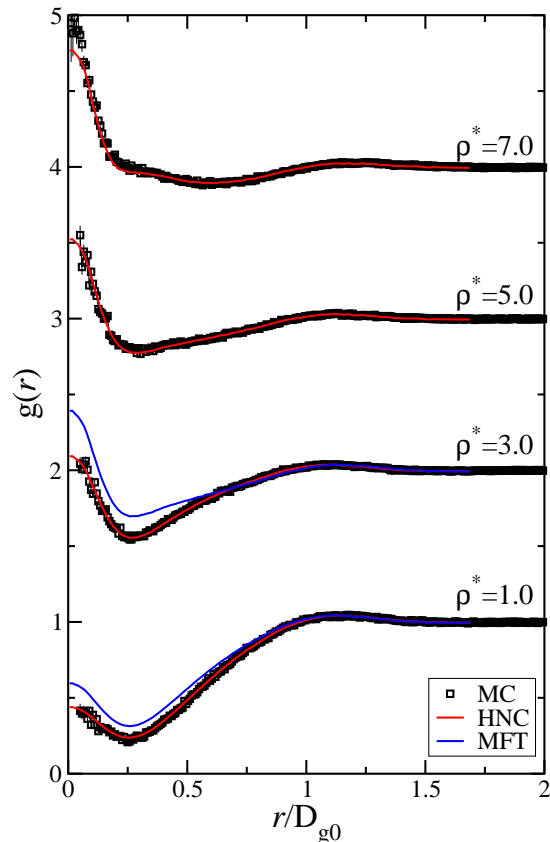


Fig. 5 The radial distribution function $g(r)$ obtained from MC simulation of the effective system, the HNC closure and the MFT approximation. The plots show results for the densities $\rho^* = 1, 3, 5$, and 7 off-set by one unit along the vertical axis. MFT-results are not shown for the highest densities for which the MFT-iteration does not converge.

5 Confinement and surface ordering

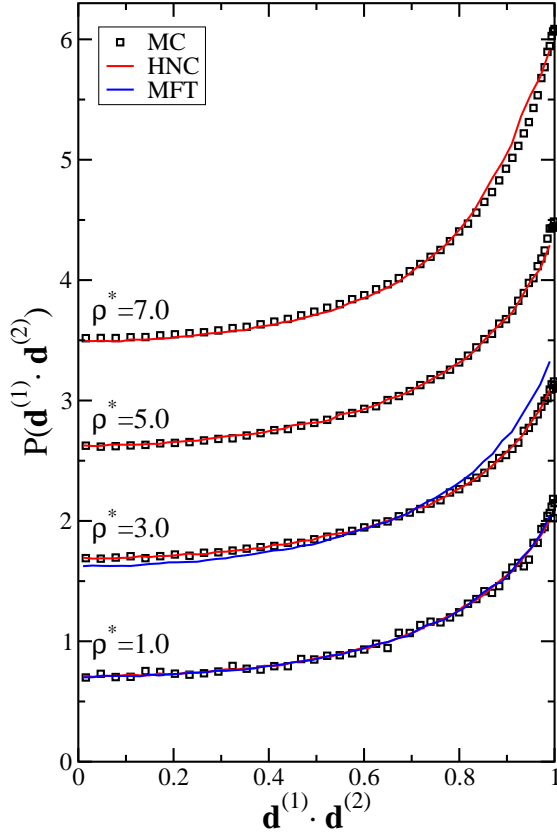
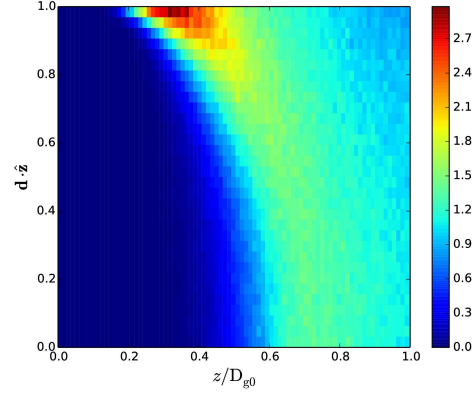


Fig. 6 Probability distribution for the scalar product between directors of nearby particles $P(\mathbf{d}^{(1)} \cdot \mathbf{d}^{(2)})$ from a MC simulation of the effective system (MC), density functional theory employing the HNC closure (HNC) and the MFT approximation (MFT). The plots show results for the densities $\rho^* = 1, 3, 5$, and 7 off-set by one unit along the vertical axis.

MC:



DFT:

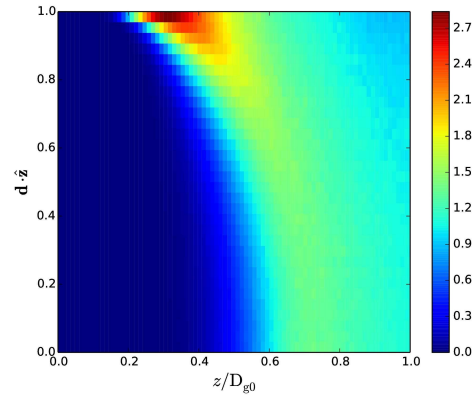
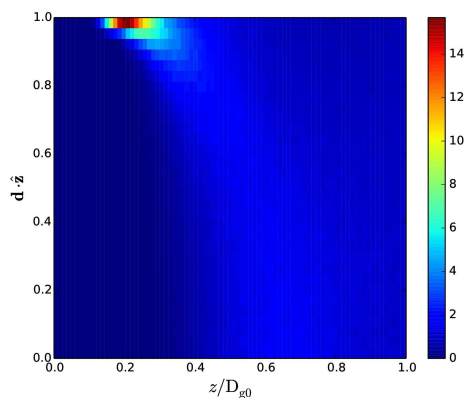


Fig. 7 The one-particle density profile scaled over the bulk value, $\rho^{(1)}(z, \mathbf{d} \cdot \hat{\mathbf{z}})/\rho$, in the presence of a wall for bulk density $\rho^* = 1$. The panels correspond to results from MC simulations and DFT, as indicated in the legends.

Within the DFT approach in the presence of the wall, we obtain the full position- and orientation dependent equilibrium one-particle density $\rho^{(1)}(z, \cos \theta)$, which minimizes the free energy functional of the system for a given temperature T and chemical potential μ ; alternatively, we can work with the bulk density ρ^* far away from the wall, as an equivalent parameter to μ . The one-particle density $\rho^{(1)}(z, \cos \theta)$ is a measure of the probability to find a particle at a distance z from the wall with its director \mathbf{d} oriented relatively to the wall normal $\hat{\mathbf{z}}$ in such a way that $\mathbf{d} \cdot \hat{\mathbf{z}} = \cos \theta$. Since the bulk is a uniform and isotropic phase, $\rho^{(1)}(z, \cos \theta) \rightarrow \rho$ for $z \rightarrow \infty$; practically, bulk is reached at a separation of a few molecular sizes from the wall.

MC:



DFT:

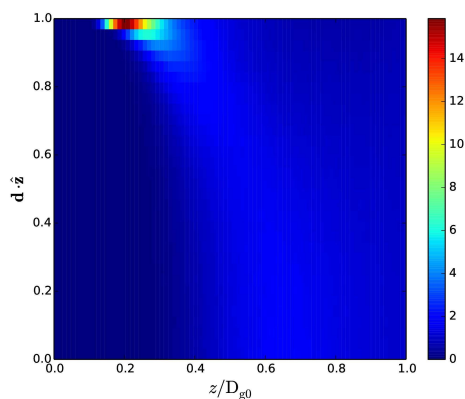


Fig. 8 Same as Figs. 7 but for bulk density $\rho^* = 5$.

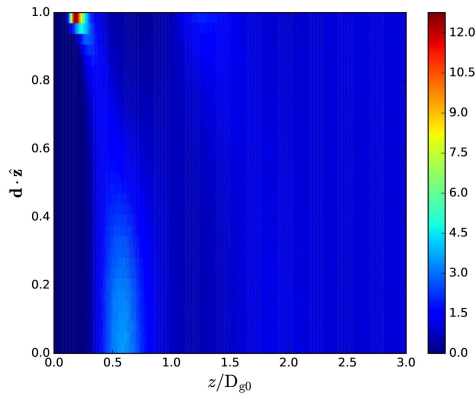
In Figs. 7 and 8, we present results for the one-particle density $\rho^{(1)}(z, \cos \theta)$ at bulk densities $\rho^* = 1$ and 5, respectively. The plots indicate the magnitude of density profile scaled over the bulk value of the same for a region close to the wall ($z < D_{g0}$), beyond which the deviations from the bulk are insignificant. Both the MC-results and the DFT predictions obtained by numerically solving Eq. (12) are shown, i.e., the DFT results pertain to the quadratic functional with HNC bulk input. For the MC simulations the box is large enough such that the system converges to the bulk state in the middle of the box. Up to $\rho^* = 5$ the results of simulations and DFT are in very good agreement and show a system where the density profile has a pronounced maximum close to the wall ($z \cong 0.2D_{g,0}$), where in addition the rings prefer to orient such that their directors stand perpendicular to the wall, $\mathbf{d} \cdot \hat{\mathbf{z}} = 1$. This corresponds to planar anchoring and, indeed, a comparison with Fig. 4 readily demonstrates that at a separation $z \cong 0.2D_{g,0}$ the planar orientation wall-disc potential is of order of the thermal energy. Wall-particle separations closer than this are forbidden due to the strong repulsions between wall and ring, whose range grows as the rings change their orientation, gradually, from planar ($\mathbf{d} \cdot \hat{\mathbf{z}} = 1$) to homeotropic ($\mathbf{d} \cdot \hat{\mathbf{z}} = 0$).

Employing the mean-field theory (MFT) approach (results not shown) brings forward density profiles that are as well consistent with this description for $\rho^* \leq 4$. However, in the MFT, the one-particle distribution $\rho^{(1)}(z, \cos \theta)$ features a maximum that is almost a factor 2 higher than for simulations, which is consistent with the notion that MFT overemphasizes the influence of the interactions between the particles. At higher densities, the MFT is also qualitatively very different and predicts a long range layering for $\rho^* \approx 5$, where the first layer of rings is oriented such that $\mathbf{d} \cdot \hat{\mathbf{z}} \approx 0$, followed by a layer of rings with $\mathbf{d} \cdot \hat{\mathbf{z}} \approx 1$, followed by another layer of rings with $\mathbf{d} \cdot \hat{\mathbf{z}} \approx 0$, and so forth. Since the MFT seems, however, to deviate strongly from the simulation results, we do not further consider it as a reliable theoretical tool for this system.

Returning to the HNC-based functional, an unexpected and novel gradual transition takes place at bulk density $\rho^* \cong 6$. In particular, it is predicted that as the density grows beyond this value, the rings closest to the wall are no more lying flat on the wall ("face-on" or planar) but rather preferentially assume a vertical ("edge-on" or homeotropic) configuration, where their directors are oriented parallel to the wall. We observe this phenomenon for both simulations and our DFT approach, although it sets in at slightly different densities in the two approaches. In Fig. 9, we show simulation and DFT results for the profile at bulk density $\rho^* = 6.9$, which is the highest density where we have obtained convergence for the DFT scheme. It can be seen that for the DFT approach there is now a clear accumulation of rings with a homeotropic anchoring to the

wall. This result is quite surprising given that the wall itself is structureless and that the planar orientation of the rings is preferable as far as their interaction with the wall is concerned; accordingly, it can be surmised that it is the interparticle interactions and their interplay with the particle-wall interaction that bring about this crossover, an issue to which we will be returning shortly. Also in the simulations the equilibrium profile $\rho^{(1)}(z, \cos \theta)$ exhibits a local maximum at $z \cong 0.5D_{g0}$ for rings which assume a homeotropic orientation with respect to the wall, but the maximum corresponding to the rings in the planar configuration is still higher at this density. This situation finally changes at higher densities, as can be seen in Fig. 10 where a snapshot as well as the one-particle density $\rho^{(1)}(z, \cos \theta)$ is shown for a MC simulation at the reduced density $\rho^* = 8.0$.

MC:



DFT:

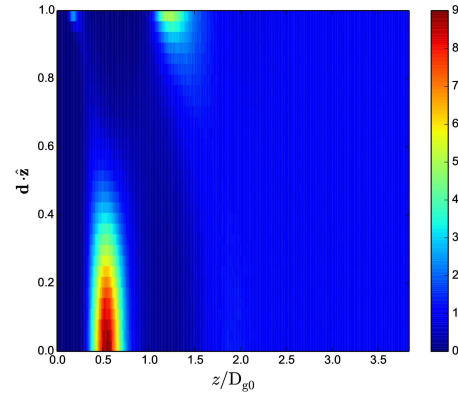
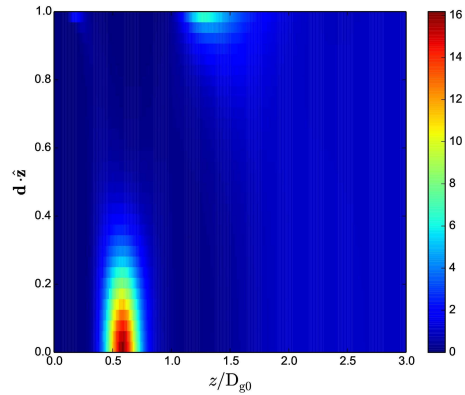


Fig. 10 Top panel: Snapshot of a MC simulation at the reduced density $\rho^* = 8$. Each coarse-grained ring is represented by a perfect circle with a diameter D_{g0} and its corresponding orientation and centers-of-mass position. Bottom panel: the corresponding scaled density profile $\rho^{(1)}(z, \mathbf{d} \cdot \hat{\mathbf{z}})/\rho$ in the presence of a wall with respect to the bulk density ρ .

Fig. 9 Same as Figs. 7 but for bulk density $\rho^* = 6.9$.

Let us first quantify the onset of the crossover of the anchoring from planar to homeotropic by introducing a suitable order parameter. We consider for this purpose the expectation value

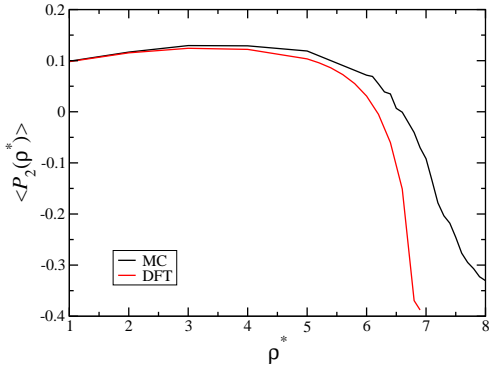


Fig. 11 Average value of the second Legendre Polynomial in $\mathbf{d} \cdot \hat{\mathbf{z}}$, $P_2(\mathbf{d} \cdot \hat{\mathbf{z}})$, for rings with a distance z from the wall that is smaller than their diameter of gyration at infinite dilution (D_{g0}) as a function of the bulk density ρ^* .

of the second-order Legendre Polynomial of $\cos \theta \equiv \mathbf{d} \cdot \hat{\mathbf{z}}$, i.e., $P_2(\cos \theta) = (3 \cos^2 \theta - 1)/2$, evaluated for all rings in a slab adjacent to the wall, $z \leq D_{g0}$, as a function of the density ρ^* . The results are shown in Fig. 11. The function changes drastically throughout the density domain where the ordering transition takes place. While the agreement between DFT predictions and simulations is very good up to $\rho^* \leq 5$, DFT predicts a more abrupt ordering transition than simulations. There is no discontinuity, cusp or nonanalytic behavior of any kind: accordingly, the flipping of the rings on the surface is not a phase transition but rather an abrupt crossover phenomenon. Nevertheless, a rapid decrease of $\langle P_2(\cos \theta) \rangle$ within a very narrow density range takes place, and its value changes from positive (planar anchoring) to negative (homeotropic anchoring) at about $\rho^* \cong 6.2$ (DFT) or $\rho^* \cong 6.5$ (MC).

It is intuitive that the particles are more likely to accumulate close to the wall, since the side of them that faces the wall has no other particles to interact with and the ring will therefore on average interact with fewer other particles. Initially, i.e., at sufficiently low densities, the rings prefer to be parallel to the wall, which is intuitive since in this configuration they will have on average less interaction partners if the rest of the configuration space is filled homogeneously with rings. Moreover, the planar orientation allows them to approach closer to the wall than the homeotropic one, leaving thus more space for the remaining rings in the z -direction. The price for the planar anchoring, however, is that the layers of planar rings experience a strong repulsion to one another due to the neighbors lying laterally along the wall, caused by the steep and longest-range effective ring-ring interaction $V_{||}(r)$ that can be seen in Fig. 2. The fact that at even higher densities the rings show

the propensity of orienting their director parallel to the wall and their surface orthogonal to it, seems to indicate that the wall-ring potential $\Phi_{\text{wall}}(z)$ combined with the anisotropic and penetrable interactions between the rings allow them to use the configuration space more efficiently and block less space for other rings, if they orient with their surface orthogonal to it. We will put this idea in more quantitative terms in what follows.

A key quantity to consider is the surface tension γ induced by the wall. The DFT approach given by Eq. (12) can be derived by carrying out a first order expansion of the first-order direct correlation function $c^{(1)}$ in density deviations $\Delta\rho^{(1)}$ with respect to the bulk system. Using the same approximation one arrives at the following expression for the surface tension γ due to the repulsive wall¹⁵:

$$\gamma = \gamma_w + \gamma_c \quad (15)$$

with

$$\begin{aligned} \gamma_w &= \frac{\rho}{2} \int dz d \cos \theta f(z, \cos \theta) \Phi_{\text{wall}}(z, \cos \theta) + \\ &\quad \frac{\rho k_B T}{2} \int dz d \cos \theta f(z, \cos \theta) \ln [f(z, \cos \theta)] - \\ &\quad \frac{\rho k_B T}{2} \int dz d \cos \theta [f(z, \cos \theta) - 1] \end{aligned} \quad (16)$$

and

$$\begin{aligned} \gamma_c &\equiv -\frac{\rho^2 k_B T}{16\pi} \int dz d \cos \theta dz' d \cos \theta' [f(z, \cos \theta) - 1] \times \\ &\quad [f(z', \cos \theta') - 1] \bar{c}(z - z', \cos \theta, \cos \theta'), \end{aligned} \quad (17)$$

where

$$f(z, \cos \theta) \equiv \rho^{(1)}(z, \cos \theta) / \rho. \quad (18)$$

The definition of \bar{c} is given in eq. (14) and corresponds to the lateral average over the direct correlation function $c(\mathbf{r}, \mathbf{d}^{(1)}, \mathbf{d}^{(2)})$ in the bulk, which we have obtained employing the HNC approximation. The term γ_w , Eq. (16), expresses the contribution of the particle-wall interactions to the surface tension, whereas the term γ_c , Eq. (17), expresses the contribution of the interparticle interactions to the same. Being surface tension terms, they both, naturally, arise from the difference between the free energy over the bulk contributions, which scale linearly with area; the ratio of this *excess* over the area are thus the two contributions to the surface tensions.

Using this formula we have computed γ and γ_c for the one-particle density $\rho^{(1)}$ obtained via the DFT approach as well as simulations and have plotted the corresponding results over the reduced density ρ^* in Fig. 12. For all investigated densities we obtain very good agreement between the results of γ computed from the $\rho^{(1)}$ distribution obtained in simulations and theory. However the ordering transition does not result

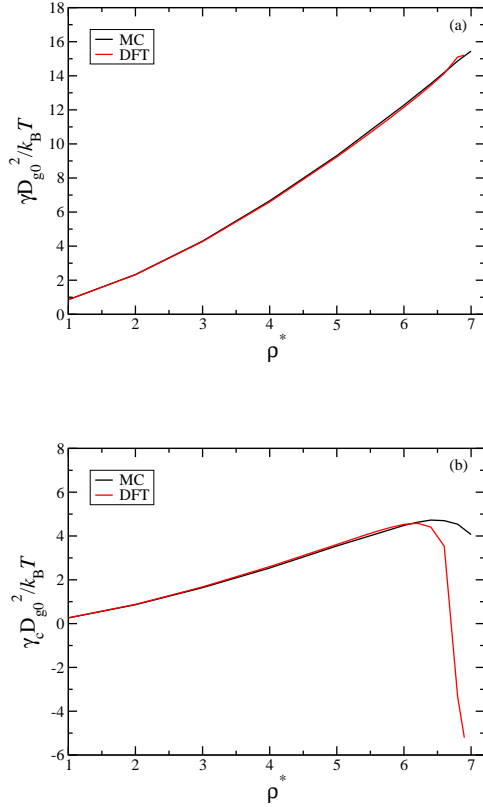


Fig. 12 (a) The total surface tension γ , Eq. (16), of a fluid of stiff ring polymers next to a planar wall, plotted against the reduced-density ρ^* . (b) The contribution γ_c , Eq. (17), to the surface tension, which is due to the inter-particle interactions.

in a significant change in the behavior of the function $\gamma(\rho^*)$, which is almost a straight line. In terms of absolute values, using a typical ring diameter $D_{g0} \cong 10$ nm and the numbers in Fig. 12(a), we obtain $\gamma \cong 10 \mu\text{N/m}$, typical of soft matter systems. For $\gamma_c(\rho^*)$ on the other hand, which is the part of the surface tension that is due to the difference in the inter-particle interaction close to the wall with respect to the bulk, we observe a radical change throughout the densities where the surface-reordering takes place. The reorientation of the effective particles leads to a significant decrease in the value of γ_c and thus the free energy due to the mutual interaction between the particles can be reduced by the reordering. This free-energy reduction is therefore the driving force behind the surface reorientation transition. By flipping up so that they stand vertically to the surface, the rings benefit from the fact that in this orientation they can take advantage of their own mutual rotations (while maintaining $\mathbf{d} \cdot \hat{\mathbf{z}} \cong 0$ in the first layer next to the wall) to assume interpenetrating orientations that drastically reduce the cost of interparticle interactions. This is accompanied by a second layer above the first, which has planar ordering, visible in both panels of Fig. 10, which, again, has an orientation perpendicular to the first layer, which is favorable for interparticle interactions at close separations. This advantage comes from the fact that the effective discs are soft and interpenetrable, i.e., it is a unique characteristic of ultra-soft anisotropic colloids, and it is dominating, at sufficiently high bulk densities, over the propensity of the wall-particle interactions to induce planar ordering. The drop in γ_c is again more abrupt for the $\rho^{(1)}$ distribution from DFT, where the ordering transition also happens at lower densities ρ^* .

6 Conclusions

We have performed a combined theoretical and computational study of the effective models arising from a coarse-graining of stiff ring polymers, putting DFT-approaches and integral equation theories in the bulk and in confinement at a strong test and examining the structural properties of isotropic ring fluids close to planar walls. We have shown that for DFT computations in the bulk MFT strongly overestimates the strength of the interactions, while the application of the HNC closure to anisotropic systems offers a description which is in very good agreement with simulation results for all densities investigated ($\rho^* \leq 7$). The HNC approach in the bulk gives us a prediction for the full anisotropic pair-correlation function $g(\mathbf{r}, \mathbf{d}^{(1)}, \mathbf{d}^{(2)})$, as well as for the direct-pair correlation function $c(\mathbf{r}, \mathbf{d}^{(1)}, \mathbf{d}^{(2)})$. The latter is useful to apply DFT in order to predict the one-particle density of rings in the vicinity of a wall. We found that by increasing the density one can induce a reorientation of the effective near-wall rings, which prefer to orient themselves parallel to the surface (planar) for low densities ρ and reorient orthogonal to the wall (homeotropic)

for higher values of ρ . This unusual phenomenon is observed in DFT as well as in computer simulations and is in stark contrast to confined hard discs, where the surface structure is mostly controlled by the interaction potential between the rings and the wall, while density has little effect. Future directions will focus on the occurrence of ordered phases (nematic or columnar) and on the behavior of such systems under non-equilibrium conditions, where the type of anchoring is expected to affect the rheological properties of the system, such as viscosity or transport coefficients.

Acknowledgments

This work has been supported by the Austrian Science Fund (FWF), Grant 23400-N16 and by the Austrian Science Fund (FWF) within the project F41 (SFB ViCoM). SAE and CNL gratefully acknowledge the Erwin Schrödinger International Institute for Mathematics and Physics for a Research in Teams Grant within the Programme RiT_2016.

A Monomer-resolved Model

We here give a brief overview of the main characteristics of the underlying monomer-resolved model that was introduced in Ref.¹³ and is employed to obtain the effective interactions between two rings as well as that between a ring and the wall. The model is based on the original bead-spring model developed by Kremer and Grest²⁶ for polymeric chains, in which the monomeric units interact via the truncated and shifted Lennard-Jones potential

$$V_{\text{LJ}}(r) = \begin{cases} 4\epsilon \left[\left(\frac{\sigma}{r}\right)^{12} - \left(\frac{\sigma}{r}\right)^6 + \frac{1}{4} \right] & \text{if } r < 2^{1/6}\sigma; \\ 0 & \text{if } r \geq 2^{1/6}\sigma. \end{cases} \quad (19)$$

This interaction is purely repulsive in nature and mimics the monomer excluded volume interactions. The connectivity in the chain, in our case the ring polymer, is enforced by a finitely extensible non-linear elastic potential (FENE)

$$V_{\text{FENE}}(r) = -\frac{kR_0^2}{2} \ln \left[1 - \left(\frac{r}{R_0}\right)^2 \right]. \quad (20)$$

The last ingredient that is added is an additional bending potential that allows us to control the rigidity of the polymer

$$V_{\text{bend}}(\theta) = \kappa(1 - \cos \theta)^2, \quad (21)$$

where θ is the angle between two consecutive bond vectors and penalizes any deviation from the straight connections. Here, we focus entirely on small rings composed on $N = 50$ monomers and have chosen the interaction parameters for the rings to be $\epsilon = k_B T$, $k = 30k_B T / \sigma^2$, $R_0 = 1.5\sigma$

and $\kappa = 30k_B T$, where k_B is the Boltzmann constant and T the temperature.

These rings are semi-flexible with a ratio of contour length over persistence length $l/l_p \cong 6.7$. This particular choice of parameters also ensures that the crossing of chains is prohibited and hence that the topology of the system is automatically preserved to remain non-concatenated.

Finally, it should be pointed out that such a polymeric system is assumed to be embedded in a good quality solvent. The solvent is treated in an implicit fashion, i.e., the interaction between monomers, and consequently also rings on the coarse-grained level, are solvent-mediated in nature.

B Numerical solution of the self consistent equations

The self consistency equations which we need to solve to compute the bulk structure of the anisotropic effective fluid employing the HNC, Eq. (7), and MFT, Eq. (10), approximations, respectively, are of the form

$$h(\mathbf{r}, \mathbf{d}^{(1)}, \mathbf{d}^{(2)}) = \mathcal{F}[h](\mathbf{r}, \mathbf{d}^{(1)}, \mathbf{d}^{(2)}), \quad (22)$$

where \mathcal{F} is a functional of h and a function of $(\mathbf{r}, \mathbf{d}^{(1)}, \mathbf{d}^{(2)})$. We solve these equations numerically via an iterative scheme that starts with some initial *guess* function f_0 and where successive iterations are computed as

$$f_{n+1} = f_n + \Delta s (\mathcal{F}[f_n] - f_n). \quad (23)$$

The mixing parameter $\Delta s > 0$ is usually set to a value smaller than 1. When applying this iterative scheme, we hope that f_n converges to a function that solves Eq. (22). Whether or not the iteration scheme converges also depends on the size of Δs . If one chooses Δs too large the scheme might not converge, however if Δs is very small one progresses in very small steps and will therefore need to carry out many iterations. For all the applications in this work we have obtained convergence with the choice $\Delta s = 0.1$. For the initial *guess* function f_0 we have chosen a flat profile for $\rho^* = 0$ and have then increased the density in small steps of $\Delta \rho^* = 0.2$ and used the solution for $\rho^* - \Delta \rho^*$ as the initial condition for the iterative scheme at density ρ^* . Since the numerical evaluation of the integrals arising in the functional \mathcal{F} is computationally demanding, we discuss their computation in more detail.

The integrals appearing in the functional \mathcal{F} are of the form:

$$f * h(\mathbf{r}, \mathbf{d}^{(1)}, \mathbf{d}^{(2)}) \equiv \int d\mathbf{x} d\Omega f(\mathbf{x}, \mathbf{d}^{(1)}, \mathbf{d}) h(\mathbf{r} - \mathbf{x}, \mathbf{d}, \mathbf{d}^{(2)}), \quad (24)$$

where $\int d\Omega$ denotes the integration over the director \mathbf{d} . We will refer to this expression as an *anisotropic convolution*. The functions f and h both exhibit a rotational symmetry, i.e.:

$$f(R\mathbf{r}, R\mathbf{d}^{(1)}, R\mathbf{d}^{(2)}) = f(\mathbf{r}, \mathbf{d}^{(1)}, \mathbf{d}^{(2)}), \quad (25)$$

where R is an arbitrary rotation matrix. The anisotropic convolution $f * h$ is therefore also rotationally symmetric and it is sufficient to compute $f * h$ for the particular choice $\mathbf{d}^{(1)} = \hat{\mathbf{z}}$ and $\mathbf{d}^{(2)} = \sin \psi \hat{\mathbf{x}} + \cos \psi \hat{\mathbf{z}}$, since it is always possible to find a choice for R , \mathbf{s} and $\cos \psi$ such that

$$(\mathbf{r}, \mathbf{d}^{(1)}, \mathbf{d}^{(2)}) = (R\mathbf{s}, R\hat{\mathbf{z}}, \sin \psi R\hat{\mathbf{x}} + \cos \psi R\hat{\mathbf{z}}). \quad (26)$$

In other words, we can choose the direction of $\mathbf{d}^{(1)}$ as the $\hat{\mathbf{z}}$ -axis and also define the plane spanned by the directors $\mathbf{d}^{(1)}$ and $\mathbf{d}^{(2)}$ as the $x-z$ -plane, rotating along the vector \mathbf{r} onto the vector \mathbf{s} . Knowledge of $f * h(\mathbf{s}, \hat{\mathbf{z}}, \sin \psi \hat{\mathbf{x}} + \cos \psi \hat{\mathbf{z}})$ therefore allows for the reconstruction of the entire function $f * h$ and we are left with the computation of

$$f * h(\mathbf{s}, \cos \psi) \equiv \int d \cos \theta d \varphi \int dt f(\mathbf{t}, \hat{\mathbf{z}}, \mathbf{d}) h(\mathbf{s} - \mathbf{t}, \mathbf{d}, \sin \psi \hat{\mathbf{x}} + \cos \psi \hat{\mathbf{z}}). \quad (27)$$

The integration over the angular coordinates of \mathbf{d} is denoted by $\int d \cos \theta d \varphi$. The inner integration corresponds to a three dimensional convolution over two functions that do not exhibit spherical symmetry. Using the convolution theorem

$$\widetilde{f * h}(\mathbf{k}) = \widetilde{f}(\mathbf{k}) \widetilde{h}(\mathbf{k}), \quad (28)$$

where $\widetilde{f}(\mathbf{k})$ is the Fourier transformed of the function $f(\mathbf{r}, \mathbf{d}^{(1)}, \mathbf{d}^{(2)})$ with respect to \mathbf{r} , we can thus carry out the inner integral with computational complexity of $\mathcal{O}(N_r^3 \log N_r)$, where N_r is the number of grid points in which we have discretized the three dimensions of \mathbf{r} . To this end, we approximate the Fourier transformations in the convolution theorem by Fourier series coefficients, which we can compute using the Fast Fourier Transform algorithm. The functions which are to be convoluted depend on \mathbf{d} and $\cos \psi$. When we carry out the integration over $d \cos \theta d \varphi$ we discretize $\cos \theta$ and φ within $N_{\cos \theta}$ and N_φ intervals, while $\cos \psi$ is discretized within $N_{\cos \psi}$ bins. In total we thus need to carry out a number of $\mathcal{O}(N_{\cos \psi} N_{\cos \theta} N_\varphi N_r^3 \log N_r)$ computations to evaluate the anisotropic convolution $f * h$. Because all the functions remain invariant if we flip an individual director, it is sufficient to compute two times the integration over $\cos \theta \in [0, 1]$ for $\cos \psi \in [0, 1]$. We have used $N_{\cos \psi}, N_{\cos \theta}, N_\varphi = 8$ and $N_r = 32$ discretization points for all iterations.

Due to rotational symmetry the functions f , h and $f * h$ are only four-dimensional instead of seven-dimensional. We have originally tabulated these functions using the effective variables $(r, \cos \theta_1, \cos \theta_2, \varphi)$ defined in Eq. (2), i.e., any given combination $(\mathbf{r}, \mathbf{d}^{(1)}, \mathbf{d}^{(2)})$ is represented by its corresponding point $(r, \cos \theta_1, \cos \theta_2, \varphi)$ in a four-dimensional grid, in which only the magnitude of \mathbf{r} and relative orientations show up. If one knows the functions f and h at these effective coordinates, one can in principle evaluate them for all

values of $(\mathbf{r}, \mathbf{d}^{(1)}, \mathbf{d}^{(2)})$ due to rotational symmetry. However we only know the function values on a rectangular grid in the effective variables, and if we for instance need to evaluate $f(\mathbf{s}, \hat{\mathbf{z}}, \sin \psi \hat{\mathbf{x}} + \cos \psi \hat{\mathbf{z}})$ at a grid point in $(\mathbf{s}, \cos \psi)$ space, the corresponding point in the effective coordinates $(r, \cos \theta_1, \cos \theta_2, \varphi)$ will in general not lie directly on the grid. We have used linear interpolation to evaluate the function on a grid point in the $(\mathbf{s}, \cos \psi)$ variables with the tabulated function values on the grid in $(r, \cos \theta_1, \cos \theta_2, \varphi)$ space. In general, we use linear interpolation in this way to transform the functions between different representations of their collective variables.

The self-consistency condition for the inhomogeneous density profile, Eq. (12), which we have employed to derive the surface-ordering of rings close to the wall is of the form

$$\rho^{(1)}(z, \cos \theta) = \mathcal{G}[\rho^{(1)}](z, \cos \theta) \quad (29)$$

and it has been solved with the same iterative scheme that we employed to compute the solution of Eq. (22). Fortunately the functional $\mathcal{G}[\rho^{(1)}]$ is numerically much easier to evaluate than $\mathcal{F}[h]$, since the function $\rho^{(1)}$ has less degrees of freedom than h . In particular, the spatial convolution appearing in Eq. (12) is merely one-dimensional and it can be easily carried out for every value of the second variable, $\cos \theta$, which is tabulated on a grid.

References

- 1 K. Binder, J. Horbach, R. Vink, and A. DeVirgiliis, *Soft Matter* **4**, 1555 (2008).
- 2 P. Huber, *J. Phys. Cond. Matt.* **27**, 103102 (2015).
- 3 L. Harnau and S. Dietrich, *Inhomogeneous Platelet and Rod Fluids*, vol 3 of *Soft Matter*, chapter 4, pp 156-311, Wiley-VCH, Berlin, (2006).
- 4 R. J. Bushby and O. R. Lozman, *Curr. Opin. Colloid Interface Sci.* **7**, 343 (2002).
- 5 F. Barmes and D. J. Cleaver, *Phys. Rev. E* **69**, 061705 (2004).
- 6 L. Bellier-Castella, D. Caprion, and J. P. Ryckaert, *J. Chem. Phys.* **121**, 4874 (2004).
- 7 M. M. Piñeiro, A. Galindo, and A. O. Parry, *Soft Matter* **3**, 768 (2007).
- 8 H. Reich, M. Dijkstra, R. van Roij, and M. Schmidt, *J. Phys. Chem. B* **111**, 7825 (2007).
- 9 L. Harnau and S. Dietrich, *Phys. Rev. E* **65**, 021505 (2002).
- 10 M. Moradi, R. J. Wheatley, and A. Avazpour, *Phys. Rev. E* **72**, 061706 (2005).
- 11 T. J. Sluckin, *Physica A* **213**, 105 (1995).
- 12 J. G. Gay and B. J. Berne, *J. Chem. Phys.* **74**, 3316 (1981).

-
- 13 P. Poier, C. N. Likos, A. J. Moreno, and R. Blaak, *Macromolecules* **48**, 4983 (2015).
 - 14 Z. W. Li, L. J. Chen, Y. Zhao, and Z. Y. Lu, *J. Phys. Chem. B* **112**, 13842 (2008).
 - 15 S. A. Egorov, A. Milchev, P. Virnau, and K. Binder, *J. Chem. Phys.* **144**, 174902 (2016).
 - 16 J. P. Hansen and I. R. McDonald, *Theory of Simple Liquids, 2nd ed.* (Academic: London 1986).
 - 17 E. Rabani and S. A. Egorov, *J. Chem. Phys.* **115**, 3437 (2001).
 - 18 E. Rabani and S. A. Egorov, *J. Phys. Chem. B* **106**, 6771 (2002).
 - 19 C. G. Gray and K. E. Gubbins, *Theory of Molecular Fluids*, (Clarendon Press: Oxford 1984).
 - 20 R. Evans, *Adv. Phys.* **28**, 143 (1979).
 - 21 J. K. Percus, *Phys. Rev. Lett.* **8**, 462 (1962).
 - 22 C. N. Likos, *Riv. Nuovo Cimento* **37**, 125 (2013).
 - 23 C. N. Likos, B. M. Mladek, D. Gottwald, and G. Kahl, *J. Chem. Phys.* **126**, 224502 (2007).
 - 24 P. Poier, P. Bačová, A. J. Moreno, C. N. Likos and R. Blaak, *Soft Matter* **12**, 4805 (2016).
 - 25 M. Z. Slimani, P. Bačová, M. Bernabei, A. Narros, C. N. Likos, and A. J. Moreno, *ACS Macro Letters* **3**, 611 (2014).
 - 26 K. Kremer and G. S. Grest, *J. Chem. Phys.* **92**, 5057 (1990).

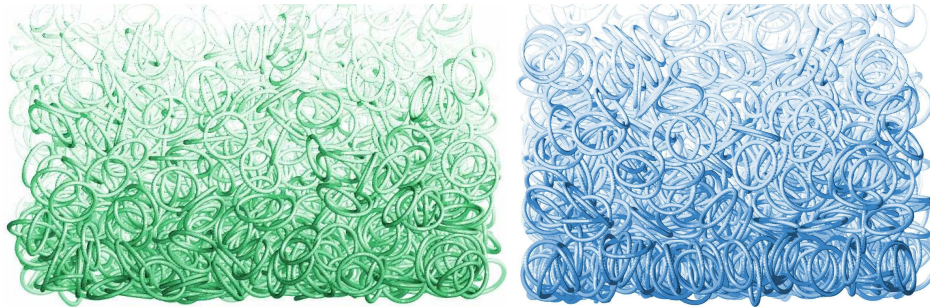


Fig. 13 TOC figure: Simulation snapshot showing a system of ultrasoft discs before (green) and after (blue) the density induced surface ordering transition.